Computer Physics Communications 246 (2020) 106867

Contents lists available at ScienceDirect

Computer Physics Communications

journal homepage: www.elsevier.com/locate/cpc

A simple implementation of PML for second-order elastic wave equations

Mingwei Zhuang [a], Qiwei Zhan [b,c], Jianyang Zhou [d,*], Zichao Guo [a], Na Liu [a], Qing Huo Liu [b,*]

[a] Institute of Electromagnetics and Acoustics and Fujian Provincial Key Laboratory of Electromagnetic Wave Science and Detection Technology, Xiamen University, Xiamen 361005, China
[b] Department of Electrical and Computer Engineering, Duke University, Durham, NC 27708, USA
[c] Department of Civil and Environmental Engineering, Duke University, Durham, NC 27708, USA
[d] Department of Electronic Engineering, Xiamen University, Xiamen 361005, China

ARTICLE INFO

Article history:
Received 6 July 2018
Received in revised form 12 August 2019
Accepted 13 August 2019
Available online 20 August 2019

Keywords:
Second-order governing wave equations
Perfectly matched layer
First-order ordinary differential equations

ABSTRACT

When modeling time-domain elastic wave propagation in an unbound space, the standard perfectly matched layer (PML) is straightforward for the first-order partial differential equations (PDEs); by contrast, the PML requires tremendous re-constructions of the governing equations in the second-order PDE form, which is however preferable, because of much less memory and time consumption. Therefore, it is imperative to explore a simple implementation of PML for the second-order system. In this work, we first systematically extend the first-order Nearly PML (NPML) technique into second-order systems, implemented by the spectral element and finite difference time-domain algorithms. It merits the following advantages: the simplicity in implementation, by keeping the second-order PDE-based governing equations exactly the same; the efficiency in computation, by introducing a set of auxiliary ordinary differential equations (ODEs). Mathematically, this PML technique effectively hybridizes the second-order PDEs and first-order ODEs, and locally attenuates outgoing waves, thus efficiently avoid either spatial or temporal global convolutions. Numerical experiments demonstrate that the NPML for the second-order PDE has an excellent absorbing performance for elastic, anelastic and anisotropic media in terms of the absorption accuracy, implementation complexity, and computation efficiency.

1. Introduction

Numerical methods are widely used to simulate acoustic/elastic wave propagation in complex materials, such as elastic, anelastic, anisotropic anelastic and poroelastic media [1–6]. When simulating wave propagation in an open region, due to the limited computer memory and computational time, the perfectly matched layer (PML) [7,8] has been extensively used to truncate the computational domain in numerical methods. Although the numerical validations of the PML are successful, the PML still may suffer from several problems, e.g., late-time instability [9–11] and poor absorbency at grazing incidences [12,13]. Several approaches have been developed to circumvent these problems: (1) The complex frequency-shifted (CFS) PML helps increase absorbency at grazing angles but does not eliminate reflections entirely, especially in near tangential angles-of-incidence [12,13]; (2) The multiaxial PML (M-PML) method simply stretches the coordinates in all three directions, where the incident waves are absorbed in all directions with different damping profile [14]. Although the M-PML is not perfectly matched layer and will lead to a larger numerical error than PML, it stabilizes for the long-time simulation in some anisotropic materials [15].

Conventionally, PML has been implemented in first-order wave equations in both electromagnetics and elastodynamics [7,8,16–19]. For the second-order elastic wave equation, however, the traditional first-order PML cannot be applied straightforwardly [9,20]. Several progresses have been reported to extend the PML for second-order PDEs. Komatitsch and Tromp [21] developed the split-field approach implementation of PML to the second-order elastodynamics equations by splitting the displacement field into four components, resulting discrete equations are either third-order, or second-order coupled with a first-order equation. Basu and Chopra [20,22] extended an unsplit-field PML for the second-order transient elastodynamics and implemented it using an implicit time integration scheme. However, these schemes require computation of the strain fields that are obtained by coordinate transformations from the displacement gradients. The implicit time integration scheme has been replaced by an explicit scheme to improve the computational efficiency [3]. Festa and Vilotte [23] demonstrated that a velocity–stress PML formulation can be used together with a second-order displacement-based elastodynamic problem. Martin et al.

* Corresponding authors.
E-mail addresses: zhoujy@xmu.edu.cn (J. Zhou), qhliu@duke.edu (Q.H. Liu).

https://doi.org/10.1016/j.cpc.2019.106867
0010-4655/

[9] showed an unsplit-field PML technique to the second-order displacement-only equation in the SEM by coupling it to a mixed velocity–stress form. Although the memory storage and the computational efficiency have improved compared with the split-field PML method [23], the scheme still need to store both velocity and stress fields. Matzen [24] developed a novel unsplit CFS-PML formulation based on the second-order wave equations with displacement as the only unknown. The PML parameters, however, are assumed constant within each element to avoid spatial integration each time step and some potentially singular parameters in PML formulation. Xie et al. [25,26] provided a new treatment to analytically remove singular parameters in the formulation in Matzen [24]. In summary, the standard PML formulation in the second-order equations is that they require overhauling revision of the existing method of the FDTD, FEM and SEM, leading to much more computer memory and time consumptions in PML region than the physical domain. Therefore, it is imperative to develop a simple, effective, and computationally efficient PML formulation for the second-order wave equations.

Fortunately, a novel PML formulation in the first-order wave equations, referred to as the Nearly PML (NPML) has proposed for the Maxwell equation [27]. Although the NPML technique deviates from the standard PML through inexact variable change, Berenger [28] has proven NPML is mathematically equivalent to the standard PML in Cartesian coordinates, hence, the NPML is a true PML. The differences are that the NPML applies the complex stretching function directly to the physical field; while the standard PML transforms a spatial derivative with respect to the complex coordinate into Cartesian coordinates. The major advantage of the NPML technique is its simplicity in implementation because it does not modify the form of the governing wave equations, even in anisotropic material. Moreover, NPML has also been further applied to first-order acoustic, elastic wave and poroelastic equations [29–31]. The detailed advantages of the NPML over the standard PML was summarized by Berenger [28].

In this paper, the novel NPML with a simple implementation is developed for the second-order displacement-based formulation. Mathematically, the scheme is mixed, since each auxiliary equation is governed by a first-order ordinary differential equation (ODE), where the stresses are needed, but the stresses are only intermediate variables from the constitutive relation. Consequently, it locally attenuates outgoing waves, thus efficiently avoid either spatial or temporal global convolutions. The NPML differs from the standard PML technique by using fewer memory variables, i.e. 8 memory variables in 2D and 18 memory variables in 3D, even in anelastic and anisotropic material. In addition, the NPML does not change the form of the governing equations. It makes the NPML very efficient, flexible and applicable to simulate wave propagation in isotropic, anelastic and anisotropic media by the FDTD, PSTD and SEM numerical methods. The numerical solutions, including an exascale computing applied to realistic earthquake simulation, indicate that the NPML is an advantageous technique in terms of computational cost and implementation simplicity over the standard PML, especially in SEM.

2. The governing equations

In a heterogeneous elastic, anisotropic medium, the linear wave equation in 3-D Cartesian coordinates can be written as

$$\rho \partial_{tt} \mathbf{u} = \nabla \cdot \boldsymbol{\tau} + \mathbf{f} \tag{1}$$

with the constitutive relation

$$\boldsymbol{\tau} = \mathbf{C} : \boldsymbol{\varepsilon} \tag{2}$$

and the definition of the strain

$$\boldsymbol{\varepsilon} = \frac{1}{2}[\nabla \mathbf{u} + (\nabla \mathbf{u})^T] \tag{3}$$

where $\mathbf{u}$ is the displacement vector, $\boldsymbol{\tau}$ denotes the stress tensor, $\boldsymbol{\varepsilon}$ is the strain tensor; $\mathbf{C}$ is the fourth-order stiffness tensor of the elastic medium which is usually expressed by the Voigt notation C_{ij} $(i, j = 1, 2, \ldots, 6)$, ρ is the solid mass density, and $\mathbf{f}$ stands for an external source force; the ':' symbol represents a double tensorial contraction operation, and a superscript T denotes the matrix transpose.

However, the attenuation of anelastic waves usually is described by a dimensionless parameter called the quality factor Q_{ij} to characterize the wave energy dissipation. This will lead to the elastic tensor C_{ij} being complex moduli in frequency domain, where the phase velocity is related to the real part of the elastic moduli and attenuation to their imaginary part. In time domain, the viscoelastic effects can be approximated by a series of standard linear solids (SLS), and the elastic tensor C_{ij} can be rewritten as [32,33]

$$C_{ij} = C_{ij}^R[1 - \sum_{\ell=1}^{L}(1 - \frac{\tau_{ij}^{\epsilon\ell}}{\tau^{\sigma\ell}})e^{-t/\tau^{\sigma\ell}}]H(t) \tag{4}$$

where C_{ij}^R denotes the relaxed moduli and $H(t)$ is the Heaviside function. The relaxed moduli are computed from the reference moduli at a reference frequency [34,35]; $\tau_{ij}^{\epsilon\ell}$ and $\tau^{\sigma\ell}$ are the two kinds of relaxation time corresponding to strain and stress relaxation times, respectively. The E–K approach [36] is a classical technique to determine the relaxation times $\tau_{ij}^{\epsilon\ell}$ and $\tau^{\sigma\ell}$ from the quality factor Q_{ij} and reference frequency f_r. In general, three $(L = 3)$ SLS mechanical elements are sufficient for accurate simulations of attenuation in anelastic materials [37]. The constitutive relation (2) needs to be modified to avoid time convolutions in Eq. (4):

$$\boldsymbol{\tau} = \mathbf{C}^U : \boldsymbol{\varepsilon} - \mathbf{C}^R \sum_{\ell=1}^{L} \mathbf{R}^\ell \tag{5}$$

where $\mathbf{C}^U$ denotes unrelaxed moduli and $\mathbf{R}^\ell$ is a memory variable related to the L attenuation mechanisms. The unrelaxed modulus is given by

$$C_{ij}^U = C_{ij}^R[1 - \sum_{\ell=1}^{L}(1 - \frac{\tau_{ij}^{\epsilon\ell}}{\tau^{\sigma\ell}})] \tag{6}$$

The memory variables, $\mathbf{R}^\ell$, are controlled by the following auxiliary first-order partial differential equations [37]

$$\partial_t R_{ij}^\ell = -\frac{R_{ij}^\ell}{\tau^{\sigma\ell}} + \varepsilon_{ij} \Phi_{ij}^\ell \tag{7}$$

where

$$\Phi_{ij}^\ell = \frac{1}{\tau^{\sigma\ell}}(1 - \frac{\tau_{ij}^{\epsilon\ell}}{\tau^{\sigma\ell}}) \tag{8}$$

are the response function components evaluated at $t = 0$. For an isotropic viscoelastic medium, Q_{ij} can be described by the two independent parameters such as Q_p and Q_s, corresponding to the compressional wave and shear wave, respectively. The viscoelastic waves can be reduced to the purely elastic waves when $\tau_{ij}^{\epsilon\ell} = \tau^{\sigma\ell}$, thus the memory variables $\mathbf{R}^\ell$ will vanish.

3. PML in second-order wave equations

3.1. Standard perfectly matched layer

We will first briefly review the standard PML in a Cartesian coordinate system. To obtain a PML formulation for given wave equations, the complex coordinates are introduced based on the

concept of complex coordinate stretching in PML region. Transforming equation in the complex coordinate into the original Cartesian coordinates [13] yields

$$\frac{\partial}{\partial \tilde{k}} = \frac{1}{s_k}\frac{\partial}{\partial k} \quad (k = x, y, z) \tag{9}$$

where s_k is the complex stretching function that determines the characteristics of the PML. A general choice of the complex stretching function s_k is as follows [13]

$$s_k = \beta_k(k) + \frac{d_k(k)}{\alpha_k(k) + i\omega} \tag{10}$$

where $d_k(k) \geqslant 0$ is the damping profile that causes amplitude of a propagating wavefield to be reduced exponentially inside the PML domain, $\alpha_k(k) \geqslant 0$ is the frequency-shifted factor that makes the attenuation depend on frequency, thus providing a Butterworth-type filter [24], and $\beta_k(k) \geqslant 1$ is the scaling factor that causes the material anisotropic inside the PML layers and reduces the phase velocity normal to the PML layers [13]. $i^2 = -1$ and ω is the angular frequency.

Take Fourier transforms of Eqs. (1)–(3), and then transform the spatial coordinates using complex coordinate stretching. Since the external source force should be zero in the PML region, we have

$$\begin{aligned} \rho\omega^2\tilde{u}_i &= \sum_{j=1}^{3}\frac{\partial\tilde{\tau}_{ij}}{\partial\tilde{x}_j} \\ \tilde{\tau}_{ij} &= \sum_{k,l=1}^{3} C_{ijkl}\frac{\partial\tilde{u}_k}{\partial\tilde{x}_l} \end{aligned} \tag{11}$$

Note that the indices $\{i, j, k, l\}$ correspond to $\{x, y, z\}$. By substituting Eq. (9) into Eq. (11), we have

$$\rho\omega^2\tilde{u}_i = \sum_{j=1}^{3}\frac{1}{s_j}\frac{\partial\tilde{\tau}_{ij}}{\partial x_j} \tag{12a}$$

$$\tilde{\tau}_{ij} = \sum_{k,l=1}^{3} C_{ijkl}\frac{1}{s_l}\frac{\partial\tilde{u}_k}{\partial x_l} \tag{12b}$$

In order to obtain a PML formulation in the time domain based on the displacement field only, we need to reformulate the above by multiplying $s_x s_y s_z$ on both sides of Eq. (12a), and rearranging equations and transforming equations to the time domain to yield,

$$\begin{aligned} \rho\omega^2 s_x s_y s_z\tilde{u}_i &= \sum_{j=1}^{3}\frac{\partial\tilde{\tau}_{ij}}{\partial x_j} \Longrightarrow \rho L(t) * u_i = \sum_{j=1}^{3}\frac{\partial\tau_{ij}}{\partial x_j} \\ \tilde{\tau}_{ij} &= \sum_{k,l=1}^{3} C_{ijkl}\frac{s_x s_y s_z}{s_l s_k}\frac{\partial\tilde{u}_k}{\partial x_l} \Longrightarrow \tau_{ij} = \sum_{k,l=1}^{3}\bar{C}_{ijkl} * \frac{\partial u_k}{\partial x_l} \end{aligned} \tag{13}$$

where $L(t) = \mathcal{F}^{-1}[\omega^2 s_x s_y s_z]$ and $\bar{C}_{ijkl} = C_{ijkl}\mathcal{F}^{-1}[\frac{s_x s_y s_z}{s_l s_k}]$, $*$ denotes a convolution integral, and $\mathcal{F}^{-1}$ is the inverse Fourier transform. According to Xie et al. [25] method, the $L(t)$ and $\bar{C}_{ijkl}$ convolution terms can be accurately computed by a recursive convolution technique, but the expressions are still relatively complicated (Eq. (18) in Xie et al. [25]). Hence, the standard PML cannot be implemented easily for the second-order displacement wave equations. It requires extensive re-construction of the existing numerical method in order to introduce the PML technique to a second-order system.

3.2. Nearly perfectly matched layer

According to Cummer [27], the idea of the NPML is to shift the complex stretching function directly from the outside of spatial partial derivatives to the physical field. This variable change is not strictly correct because the complex stretching function varies with space, but this change does not substantially affect the NPML performance. Hence, Eq. (12) needs to be rewritten in the NPML formulation to become

$$\begin{aligned} \rho\omega^2\tilde{u}_i &= \sum_{j=1}^{3}\frac{\partial\frac{1}{s_j}\tilde{\tau}_{ij}}{\partial x_j} \\ \tilde{\tau}_{ij} &= \sum_{k,l=1}^{3} C_{ijkl}\frac{\partial\frac{1}{s_l}\tilde{u}_k}{\partial x_l} \end{aligned} \tag{14}$$

Next, we will prove the NPML is fundamentally equivalent to the standard PML. Multiplying the $\frac{1}{s_x s_y s_z}$ on both sides of Eq. (14) leads to

$$\begin{aligned} \frac{1}{s_x s_y s_z}\rho\omega^2\tilde{u}_i &= \sum_{j=1}^{3}\frac{1}{s_x s_y s_z}\frac{\partial\frac{1}{s_j}\tilde{\tau}_{ij}}{\partial x_j} \\ \frac{1}{s_x s_y s_z}\tilde{\tau}_{ij} &= \sum_{k,l=1}^{3} C_{ijkl}\frac{1}{s_x s_y s_z}\frac{\partial\frac{1}{s_l}\tilde{u}_k}{\partial x_l} \end{aligned} \tag{15}$$

Note that we can always find two stretched coordinate functions that are independent with the spatial partial derivatives on the right-hand side of Eq. (15). Then we can reconstruct the NPML formulation as

$$\begin{aligned} \rho\omega^2\bar{\tilde{u}}_i &= \sum_{j=1}^{3}\frac{1}{s_j}\frac{\partial\bar{\tilde{\tau}}_{ij}}{\partial x_j} \\ \bar{\tilde{\tau}}_{ij} &= \sum_{k,l=1}^{3} C_{ijkl}\frac{1}{s_l}\frac{\partial\bar{\tilde{u}}_k}{\partial x_l} \\ \bar{\tilde{u}}_i &= \frac{\tilde{u}_i}{s_x s_y s_z} \\ \bar{\tilde{\tau}}_{ij} &= \frac{\tilde{\tau}_{ij}}{s_x s_y s_z} \end{aligned} \tag{16}$$

Comparing Eq. (16) with Eq. (12), we find that they are in similar expressions except that all the physical fields in the NPML region are multiplied by the stretched coordinate function in all three directions. The differences are that the standard PML is the equation of the $\tilde{u}_i$ and $\tilde{\tau}_{ij}$ in the PML region, while the NPML is the equation of the $\bar{\tilde{u}}_i$ and $\bar{\tilde{\tau}}_{ij}$. Since the stretched coordinate function is the one at the NPML interface to the physical region, it ensures continuity of the $\bar{\tilde{u}}_i$ and $\bar{\tilde{\tau}}_{ij}$ across this interface. Hence, the NPML and standard PML formulations are thus equivalent under this variable change. Transforming equation (14) to the time domain and rearranging them, we obtain the following

$$\begin{aligned} \rho\frac{\partial^2 u_i}{dt^2} &= \sum_{j=1}^{3}\frac{\partial\bar{\tau}_{ij}}{\partial x_j} \\ \tau_{ij} &= \sum_{k,l=1}^{3} C_{ijkl}\frac{\partial\bar{u}_{kl}}{\partial x_l} \end{aligned} \tag{17}$$

where

$$\begin{aligned} \bar{\tau}_{ij} &= \frac{1}{s_j}\tau_{ij} \\ \bar{u}_{kl} &= \frac{1}{s_l}u_k \end{aligned} \tag{18}$$

By introducing 18 auxiliary variables, Eq. (18) can easily be solved in NPML layers. The auxiliary differential equation was described

Table 1
PML auxiliary variables in acoustic and elastic wave equations.

	NPML		PML in specfem3D	
	Acoustic	Elastic	Acoustic	Elastic
2D	4	8	6	12
3D	6	18	12	39

by Zhang and Shen [13], as follows

$$\begin{aligned} &\bar{F} = \frac{1}{s_k}F = \frac{1}{\beta_k}(F - T) \\ &\frac{\partial T}{\partial t} + (\alpha_k + \frac{d_k}{\beta_k})T = \frac{d_k}{\beta_k}F \end{aligned} \tag{19}$$

where F denotes displacement or stress fields, T is an auxiliary variable controlled by the first-order ODE. According to Zhang and Shen [13], d_k, β_k and α_k can be chosen as polynomial functions in the NPML layer,

$$\begin{aligned} d_k &= d_0 \left(\frac{k}{L}\right)^{p_d} \\ \beta_k &= 1 + (\beta_0 - 1)\left(\frac{k}{L}\right)^{p_\beta} \\ \alpha_k &= \alpha_0 \left[1 - \left(\frac{k}{L}\right)^{p_\alpha}\right] \\ d_0 &= -\frac{(p_d + 1)v}{2L} \ln R_0 \end{aligned} \tag{20}$$

where L is the thickness of the NPML layer in the k direction, d_0, β_0 and α_0 are the maximum values of d, β and α. Generally, the degree of a polynomial p_d, p_β and p_α range form zero to four. R_0 is the reflection coefficient at normal incidence at the exterior boundary, and v is the maximum propagation speed in the NPML layer.

Table 1 gives a comparison of the auxiliary variables of the NPML method with that of the standard PML in 2-D or 3-D wave equations [25,26]. It is noteworthy that Kaltenbacher et al. [38] introduced an efficient PML for the second-order acoustic wave equations, in which there are only 3 auxiliary variables in 2D and 4 auxiliary variables in 3D. Finally, we summarize the advantages of this NPML formulation for the second-order wave equations: (1) By introducing some auxiliary variables, the NPML formulation in Eq. (17) does not change the form of the governing equations. It makes the NPML very efficient and flexible to simulate wave propagation in unbounded media. (2) As the NPML technique does not depend on the properties of the underlying material, it is suitable for isotropic, viscoelastic, anisotropic media, and even anisotropic anelastic media. (3) All the auxiliary equations are first-order ODEs, so they can easily be solved to ensure high computationally efficiency in NPML layers.

4. Numerical methods

The NPML technique proposed above has been implemented in the SEM and FDTD method. To verify the accuracy, efficiency and robustness of the NPML with numerical simulations, we use the SEM and FDTD method to simulate seismic wave propagation in an unbounded domain with complex media.

The staggered-grid FDTD method has been widely used for modeling seismic wave propagation in complex media. The main advantages of the FDTD method are its intrinsic simplicity and robustness when modeling complex structures. The staggered-grid displacement-based FDTD scheme was then used by Ohminato and Chouet [39],Moczo et al. [40]. The displacement-based scheme in a 3-D problem needs only 75% of the memory required compared with the velocity–stress scheme because the stress tensor is only temporary quantities which are not stored in memory [41, p. 11]. In this paper, we discretize the displacement-based equations using the second-order central differencing scheme for space and time.

The spectral element method was introduced to simulate wave propagation in seismology [2,21,42]. This method combines the advantages of the pseudospectral method with those of the finite element method. That is, the accuracy and rapid convergence of the former and the geometrical flexibility of the latter. Because of the choices of Gauss–Lobatto–Legendre (GLL) points in an element, a perfectly diagonal mass matrix could be obtained, which significantly reduces the computational cost and leads to an explicit time scheme relatively easy to implement on modern computing clusters. A detailed review of the SEM in computational seismology was given by Komatitsch et al. [42]. An open computational code also has been made available as the SPECFEM3D software package by Computational Infrastructure for Geodynamics website (https://geodynamics.org/cig/software/specfem3d/). So far the PML in specfem3D can only be used to absorb wave propagation in lossless isotropic media.

5. Numerical examples

5.1. Homogeneous media

Homogeneous isotropic, viscoelastic and anisotropic models are used first to illustrate the accuracy of the NPML for second-order wave equations, and the analytical solutions are used as references. The physical domain is 1000 m × 600 m × 800 m. An point force source with the polarization direction $(\theta, \phi) = (63.4°, 36.7°)$, having a Ricker wavelet time function with the center frequency $f_0 = 15$ Hz, is located at $(400, 200, 300)$ m. A receiver is deployed at $(700, 450, 700)$ m. The computational domain is discretized using a grid 400 × 240 × 320 cells in FDTD and 50 × 30 × 40 = 60,000 elements in SEM, respectively. We use a polynomial degree $N = 4$ in each spectral element, which means that the entire model contains a total of $3,915,681$ GLL nodal points. The PML region consists of 10-layer-thick in FDTD, and 2 layers of spectral element in SEM. The damping parameters $p_d = 3$, $p_\alpha = 1$, $R_0 = 0.05\%$, $\beta_0 = 1$ and $\alpha_0 = \pi f_0$ are used in the numerical implementation. The global relative L_2-norm error of numerical solution is calculated using Eq. (21),

$$L_2 = \frac{\sqrt{\int_0^T \left[\upsilon(t) - \upsilon_{ref}(t)\right]^2 dt}}{\sqrt{\int_0^T \upsilon_{ref}(t)^2 dt}} \tag{21}$$

where υ and υ_{ref} are the numerical solutions and reference solutions, respectively.

5.1.1. Homogeneous isotropic and viscoelastic model

The P-wave velocity, S-wave velocity and density are 3000 m/s, 1900 m/s and 2500 kg/m^3, respectively. The time interval Δt of the FDTD and SEM are chosen as 0.4 ms and 0.5 ms, respectively. The calculated waveforms from the two numerical methods are compared with the analytical solutions in Fig. 1. It is shown that excellent agreement is achieved between the two numerical solutions and the analytical solutions, and the analytical expressions are given in the Appendix. The L_2 norm errors of the SEM and FDTD solutions are 0.45% and 0.57%, respectively. Fig. 2 shows the SEM wavefield energy ($E = \rho \mathbf{v}^2$, $\mathbf{v}$ is velocity vector) decay curves for isotropic media with time (0–5) s measured in the computational domain excluding the PML region. There is no instability appearing in the long-time simulation.

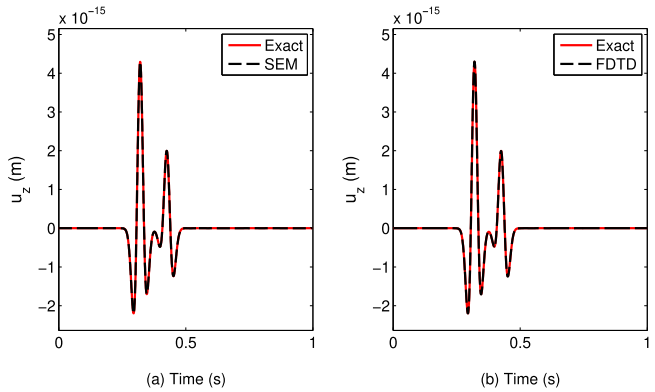

Fig. 1. Comparisons of the displacement u_z component between the numerical solutions and the analytical solutions in an isotropic material. (a) SEM and analytical solutions. (b) FDTD and analytical solutions.

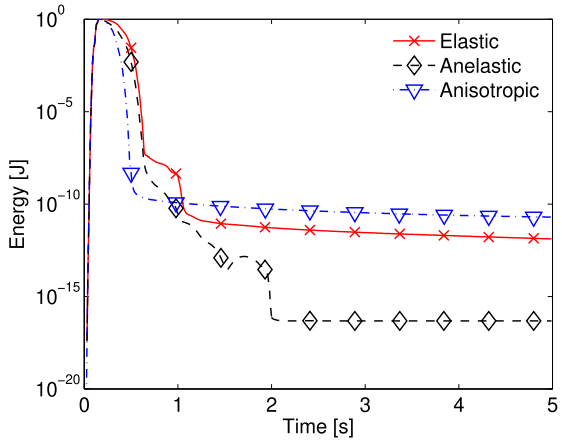

Fig. 2. Wavefield energy decay curves at the semi-logarithm scale for elastic, anelastic and anisotropic materials.

Furthermore, Table 2 shows the comparison between the NPML and standard PML (specfem3D software) for SEM in computational efficiency with 60 cores and 5000 steps. The NPML or PML region consists of two elements within the damping direction for all examples. The proportion of the NPML or PML region over the entire computational domain will decrease with the increasing number of the spectral elements. Although with the increasing of the number spectral elements, the differences of both methods are gradually reduced, the result shows that the computational efficiency of the NPML technique also raises about 30% when the proportion of PML is 5.7%. This demonstrates the high efficiency of the NPML technique, compared with the standard PML.

Table 2
Computational efficiency comparison between the NPML technique and standard PML technique.

SEM elements	N	NPML (s)	PML (s)	PML weight (%)
40 × 40 × 40	4	132	332	13.5
60 × 60 × 60	4	432	796	9.4
80 × 80 × 80	4	1001	1740	7.2
100 × 100 × 100	4	1963	2778	5.7

The attenuation model is a constant $Q_p = Q_s = 30$, which is modeled by three Zener bodies. The reference frequency is chosen as $f_r = 1$ Hz. The analytical expressions are given for anelastic media in the Appendix. Fig. 3 is the simulation result of SEM and FDTD in viscoelastic media. As shown in these figures, our simulation results have very good agreement with reference solutions. The energy decay curve of Fig. 2 also shows its superior absorbing performance in viscoelastic media. There is no instability appearing in the long-time simulation. In addition, Fig. 3(a) compares the elastic and viscoelastic models, where the strong attenuation in the anelastic medium is apparent. In Fig. 3(c), some minor spurious reflections would be observed for specfem3D package when material is anelastic. Fig. 4 illustrates the snapshots of the x-component of the displacement obtained at 0.25 s, 0.45 s and 0.625 s after using the NPML. These snapshots also indicate that the NPML has an excellent absorbing performance.

5.1.2. Homogeneous anisotropic model

In this case we will validate the NPML for anisotropic media in SEM. The analytical expression can be found in Wang and Achenbach [43]. A monoclinic ($NaAlSi_3O_8$) elasticity matrix C_{ij} is given as [44, p. 465]

$$C_{ij} = \begin{bmatrix} 74 & 36 & 39 & 0 & -6.6 & 0 \\ 36 & 131 & 31 & 0 & -13 & 0 \\ 39 & 31 & 128 & 0 & -20 & 0 \\ 0 & 0 & 0 & 17 & 0 & -2.5 \\ -6.6 & -13 & -20 & 0 & 30 & 0 \\ 0 & 0 & 0 & -2.5 & 0 & 32 \end{bmatrix} \text{GPa}$$

and the mass density is 2620 kg/m^3. The maximum and minimum propagation velocities are about 7440 m/s and 3000 m/s,

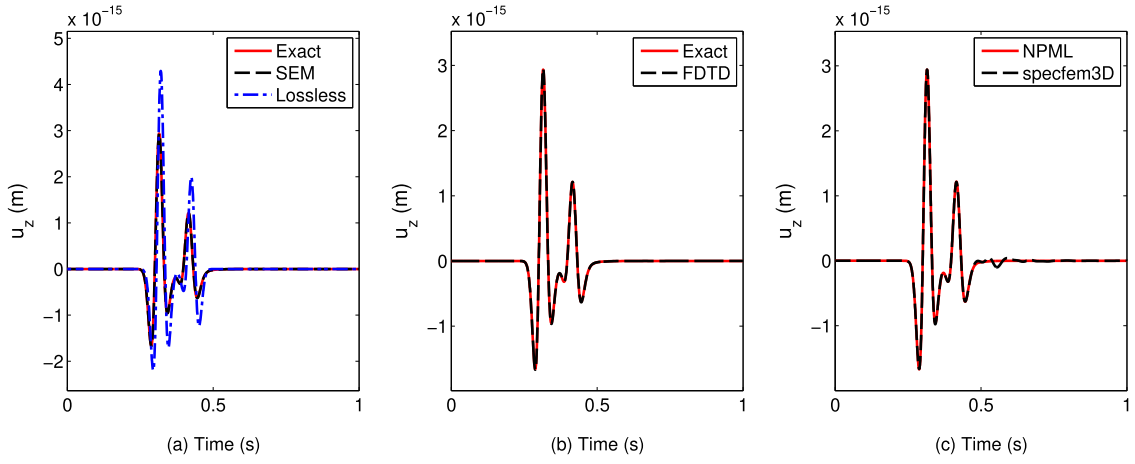

Fig. 3. Comparisons of the displacement u_z component between the numerical solutions and the analytical solutions in a viscoelastic material. (a) SEM and analytical solutions. (b) FDTD and analytical solutions. (c) NPML in SEM and specfem3D solutions.

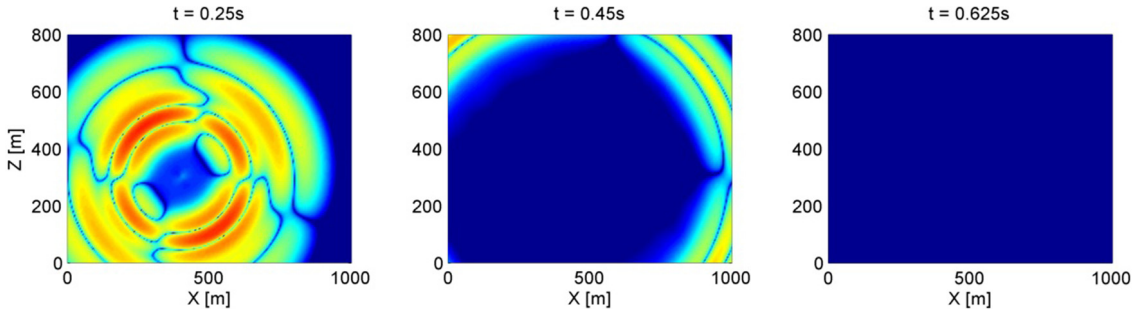

Fig. 4. The snapshots of the x-component of the displacement field at $y = 250$ m surface. (a) At time 0.25 s. (b) At time 0.45 s. (c) At time 0.625 s.

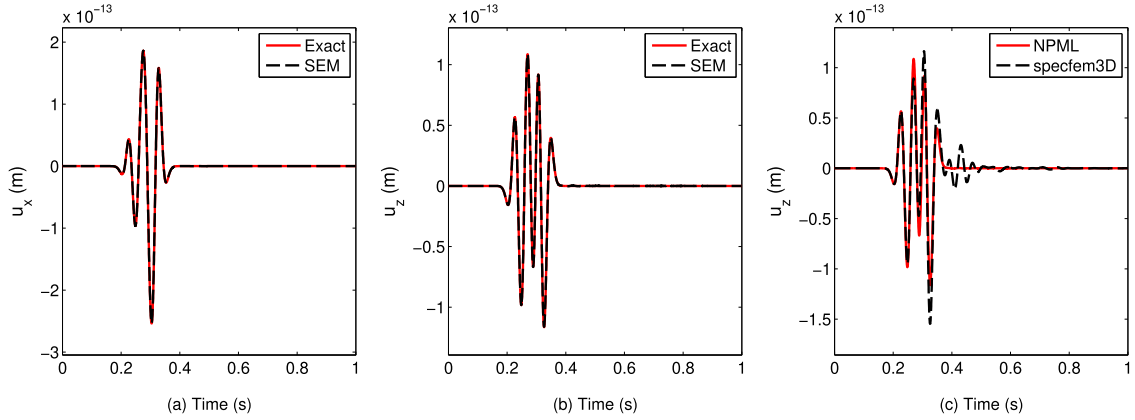

Fig. 5. Comparisons of the displacement field between the numerical solutions and the analytical solutions in a monoclinic crystal. (a) Displacement x-component. (b) Displacement z-component. (c) NPML in SEM and specfem3D solutions.

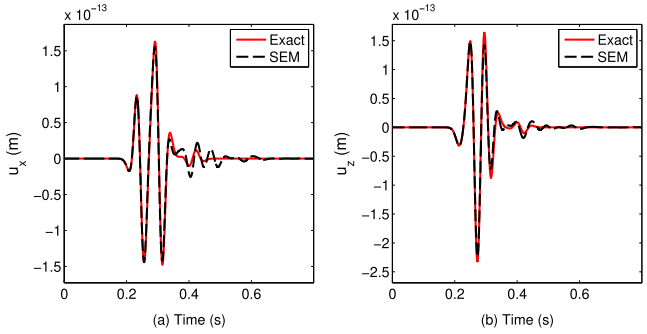

Fig. 6. Comparisons of the displacement field between the numerical solutions and the analytical solutions in a strongly anisotropic crystal. (a) Displacement x-component. (b) Displacement z-component.

respectively. The time interval Δt is chosen as 0.25 ms. Fig. 5 gives the comparisons between the SEM solutions and analytical solutions, and good agreement is achieved. The L_2 norm errors corresponding to the u_x and u_z are 0.2% and 0.3%, respectively. So far, the PML in specfem3D only works with lossless isotropic media and, therefore, the strong spurious reflections would be observed in specfem3D solutions, as shown in Fig. 5(c). At last, the energy decay curve of Fig. 2 also indicates that the NPML remains stable for long-time simulation in this anisotropic media.

A well-known problem of PML is its intrinsically instability in some anisotropic materials for long-time wave propagation. But Meza-Fajardo and Papageorgiou [14] have proposed a more general coordinate stretching method in the PML region, in which the waves are absorbed in all directions with different damping profiles

$$\begin{aligned} d_x(x,y,z) &= d_x^x + \xi_y d_x^x + \xi_z d_x^x \\ d_y(x,y,z) &= d_y^y + \xi_x d_y^y + \xi_z d_y^y \\ d_z(x,y,z) &= d_z^z + \xi_x d_z^z + \xi_y d_z^z \end{aligned} \tag{22}$$

where d_x, d_y and d_z are the classical damping profile in the x, y and z directions inside the PML, respectively. ξ_x, ξ_y and ξ_z are the ratios of the damping profiles varying between 0 and 1 inside the PML. Here, it is equally easy to introduce the multiaxial PML method to the NPML formulation. Let us use a strongly anisotropic material [45] with

$$C_{ij} = \begin{bmatrix} 10 & 3.5 & 2.5 & -5 & 0.1 & 0.3 \\ 3.5 & 8 & 1.5 & 0.2 & -0.1 & -0.15 \\ 2.5 & 1.5 & 6 & 1 & 0.4 & 0.24 \\ -5 & 0.2 & 1 & 5 & 0.35 & 0.525 \\ 0.1 & -0.1 & 0.4 & 0.35 & 4 & -1 \\ 0.3 & -0.15 & 0.24 & 0.525 & -1 & 3 \end{bmatrix} \text{ GPa}$$

and the mass density is 3200 kg/m^3. Fig. 6 gives the comparisons between the SEM solutions with $\xi_x = \xi_y = \xi_z = 0.23$ and analytical solutions. The L_2 norm errors corresponding to u_x and u_z are 13.7% and 12.4%, respectively. Note the multiaxial NPML is no longer a perfectly matched layer when $\xi_i > 0$, and the numerical error increases with the increases of the ratio of the damping profiles, but it can maintain excellent stability for the long-time simulation in this strongly anisotropic material. As indicated by the corresponding energy decay curve shown in Fig. 7, the energy quickly blows up when the damping functions are not introduced or a small amount of the damping functions are introduced. At last, the energy curve for the multiaxial NPML decays smoothly and steadily during simulation time under a suitable damping ratios.

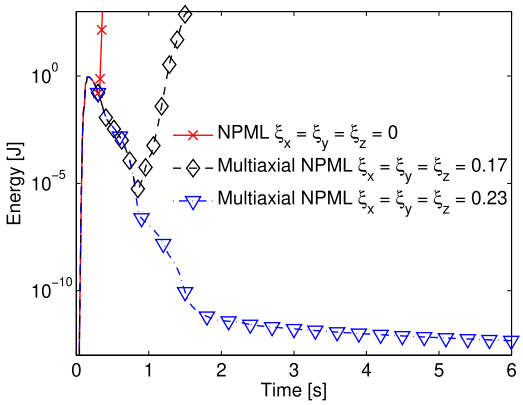

Fig. 7. Wavefield energy decay curves at the semi-logarithm scale for a strongly anisotropic crystal.

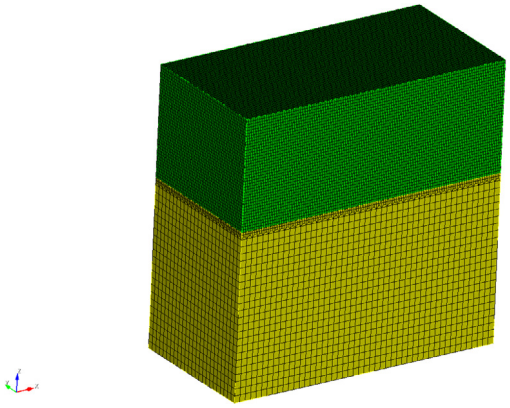

Fig. 8. A solid–fluid coupling model with an fluid layer as the top layer. A finer mesh covers the fluid layer and a coarser mesh covers the solid layer.

5.2. Coupling between acoustic and elastic waves

In this section, we consider a model with an acoustic layer on top of a homogeneous elastic layer. The analytical solution is provided by Diaz (Gar6more3D: http://gar6more3d.gforge.inria.fr/). The fluid has an acoustic wave velocity of 1500 m/s and density of 1000 kg/m^3, and the solid has a P-wave velocity of 4800 m/s, S-wave velocity of 3000 m/s and density of 2800 kg/m^3. The physical domain is [0,1000] $\times$ [0, 500] $\times$ [-600, 400] m^3. We use a Ricker wavelet with a center frequency of 40 Hz. The time interval is 0.04 ms. The source is located in the acoustic domain at $(x, y, z) = (500, 250, 75)$ m. Four receiving positions R1, R2, R3, and R4 are chosen at the following locations: $(x, y, z) = (600, 350, 200)$, $(800, 350, 200)$, $(600, 350, -200)$, $(800, 350, -300)$, respectively.

Due to the smaller propagation velocity of the fluid domain than the solid domain, it is reasonable to use finer elements to cover the fluid domain and coarser elements to cover the solid domain. The total number of unknowns in such a model can be significantly smaller than in a uniform discretization scheme. Fig. 8 shows the configuration of a solid–fluid model with meshes. The sampling density in the fluid and solid domains is approximately 8 and 6 points per wavelength (PPW) at the highest frequency $f_{max} = 110$ Hz, respectively.

A comparison between the analytical and numerical solutions at four locations is shown in Fig. 9. The excellent agreement indicates that the NPML has an excellent absorbing performance. Fig. 11 illustrates the snapshots of the z-component of the displacement obtained at 0.17 s, 0.22 s and 0.35 s. These snapshots also indicate that the NPML has an superior absorbing performance. The energy decay curve of Fig. 10 indicates that the NPML remains stable in this solid–fluid model.

5.3. A 3-D exascale realistic earthquake simulation

In this numerical experiment, we will demonstrate a more realistic 3-D case. Taiwan is well known as a seismically active zone mainly due to collisions between the Philippine Sea Plate and Eurasian Plate. An earthquake of magnitude 6.4 on the moment magnitude scale hit Hualien County on February 6, 2018, with the focal depth at about 10 km. A simplified 3-D model as shown in Fig. 12 is simulated. The simulations are performed up to 2 Hz, and the physical model includes the effects of irregular topography and the solid–fluid Taiwan strait region, as shown in Fig. 12. The elevation data of the realistic earth's surface model are produced on the NASA Shuttle Radar Topographic Mission (SRTM), and the Taiwan strait has about 100 meters in the average depth.

The physical domain is 620 km $\times$ 380 km $\times$ 37.5 km for the three-layer medium with realistic topography. The fluid has an

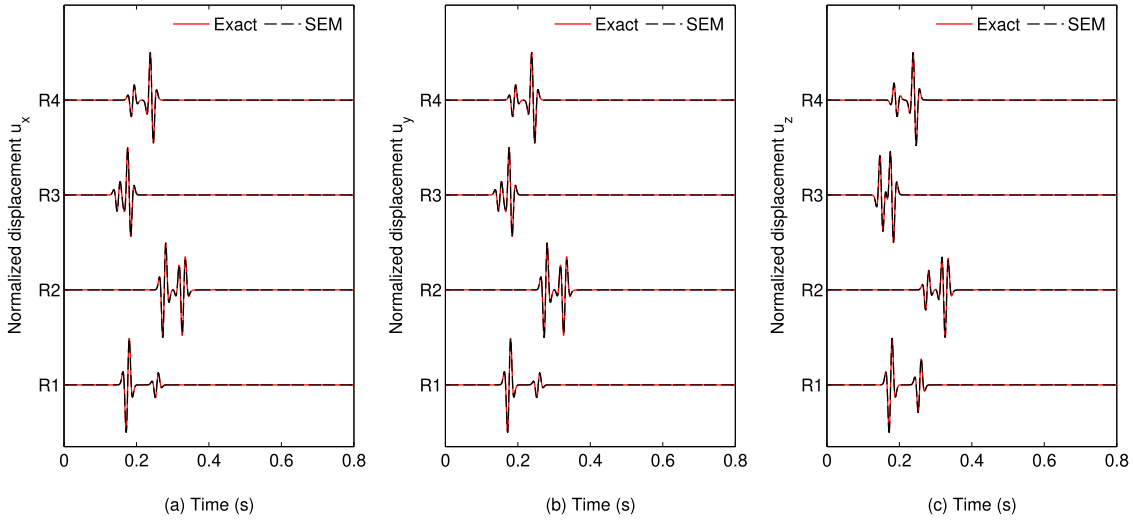

Fig. 9. Comparison between the numerical solutions and analytical solutions of the displacement field at four locations. (a) Displacement x-component; (b) Displacement y-component; (c) Displacement z-component.

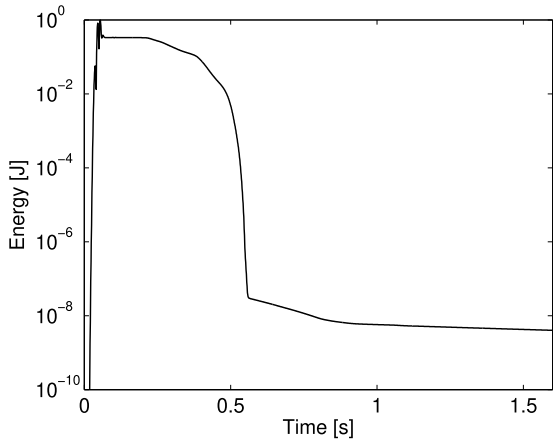

Fig. 10. Wavefield energy decay curves at the semilogarithm scale for the solid–fluid coupling model.

acoustic wave velocity of 1500 m/s and density of 1000 kg/m^3; the surface layer has a P-wave velocity of 2600 m/s, S-wave velocity of 1800 m/s and density of 2000 kg/m^3; the bottom layer has a P-wave velocity of 3200 m/s, S-wave velocity of 2100 m/s and density of 2500 kg/m^3. The moment-tensor is the classic method describing seismic sources. A moment-tensor solution be derived from (https://www.cwb.gov.tw/V7e/earthquake/seismic.htm) as

$$M = \begin{bmatrix} -210.946 & 111.798 & 83.372 \\ 111.798 & 114.781 & 132.457 \\ 83.372 & 132.457 & 96.165 \end{bmatrix} \times 1E^{16}\ \mathrm{N\cdot m}$$

The quake's epicenter is located at (518.47, 215.9, 10) km, with a Ricker source time function of maximum frequency 2 Hz. Four receivers are located on the free surface in Xiamen city (239.824, 248.124, 0) km, Taipei city (505.306, 298.150, 0) km, Sea station (297.531, 124.007, 0) and Kaohsiung city (402.056, 126.548, 0) km, respectively. The mesh used for the SEM numerical simulation is composed of 72,000,000 hexahedron elements. Two NPML absorbing layers in the damping direction are implemented on all the sides of the model except for the top free surface. The simulation parameters are listed in Table 3. All the simulations were performed on a cluster composed of 1875 cores distributed on 79 nodes with 64 Gb of memory per node.

Table 3
Simulation parameters for Hualien County earthquake model with a realistic topography in Fig. 12.

	N	GLL points (billion)	PPW	Δt (ms)	Steps	Times (h)
NPML	3	1.954	4.5	5	100,000	14.0
NPML	4	4.625	6.0	3	150,000	47.68
PML	4	4.625	6.0	3	150,000	55.74
NPML	5	9.027	7.5	2	200,000	115.34

Results of our simulations are shown in Fig. 13. To examine the convergence of the SEM solution for this 3-D model, we perform three simulations using polynomial order $N = 3, 4$ and 5, its

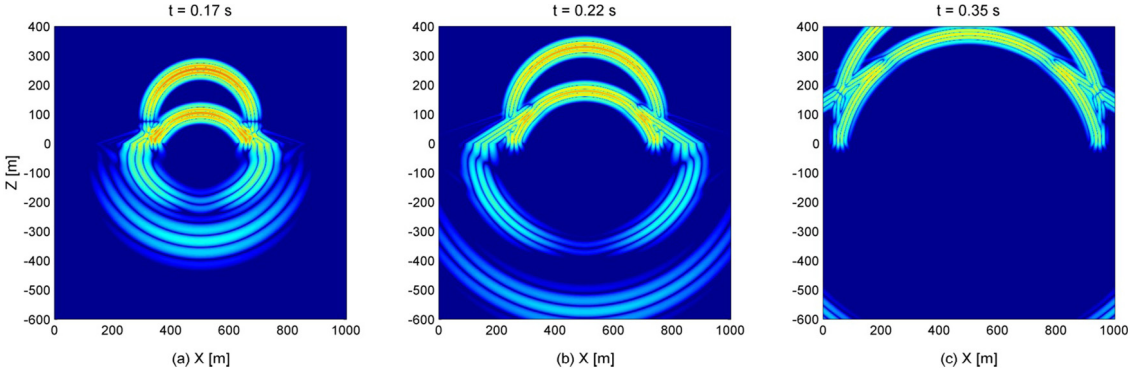

Fig. 11. The snapshots of the z-component of the displacement field at $y = 200$ m surface; (a) At time 0.17 s. (b) At time 0.22 s. (c) At time 0.35 s.

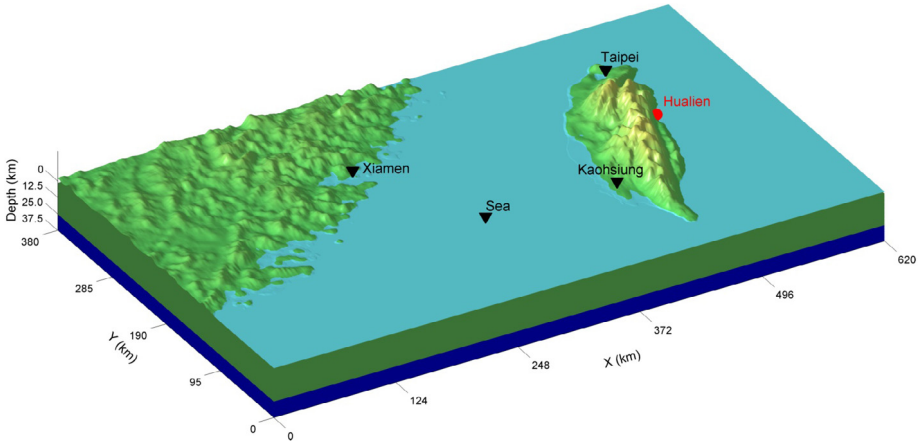

Fig. 12. Elevation map for the three-layer medium with realistic topography, and the Taiwan strait is about 100 meters in average depth. The maximum elevation is about 3000 m, a horizontal layered interface at depth 26 km. The NPML absorbing layers are applied on all the sides of the model except for the top free surface.

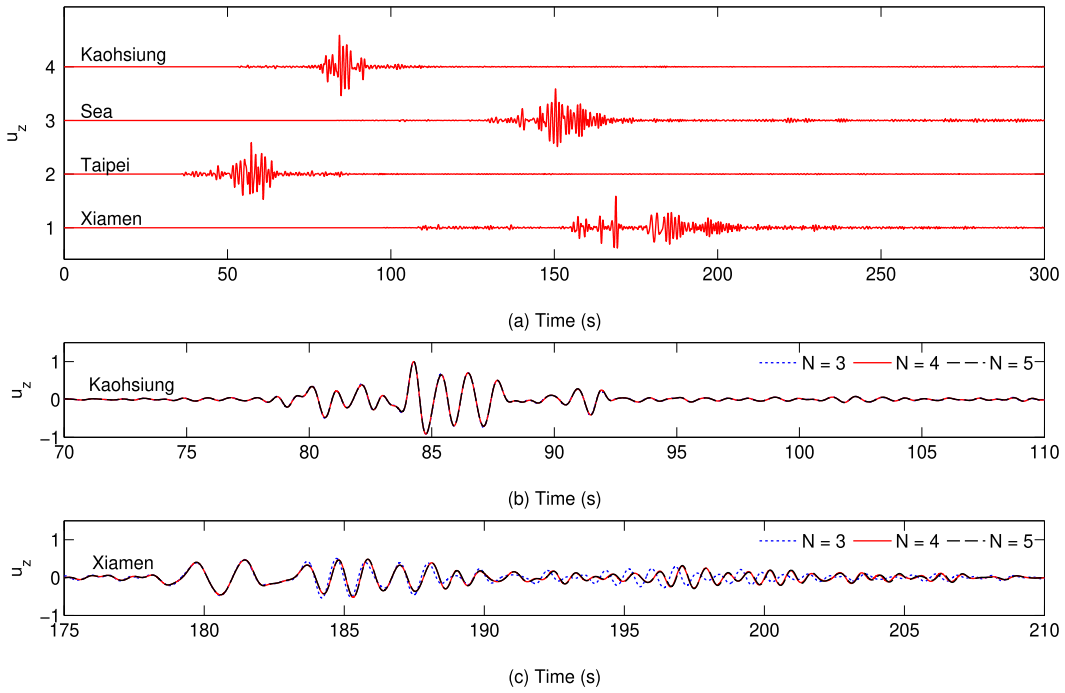

Fig. 13. Simulated ground displacement time histories for Hualien County earthquake. (a) Simulation results of the SEM with $N = 4$ for four stations. (b) Comparison of displacement time histories between different polynomial degree for Kaohsiung station. (c) Comparison of displacement time histories between different polynomial degree for Xiamen station.

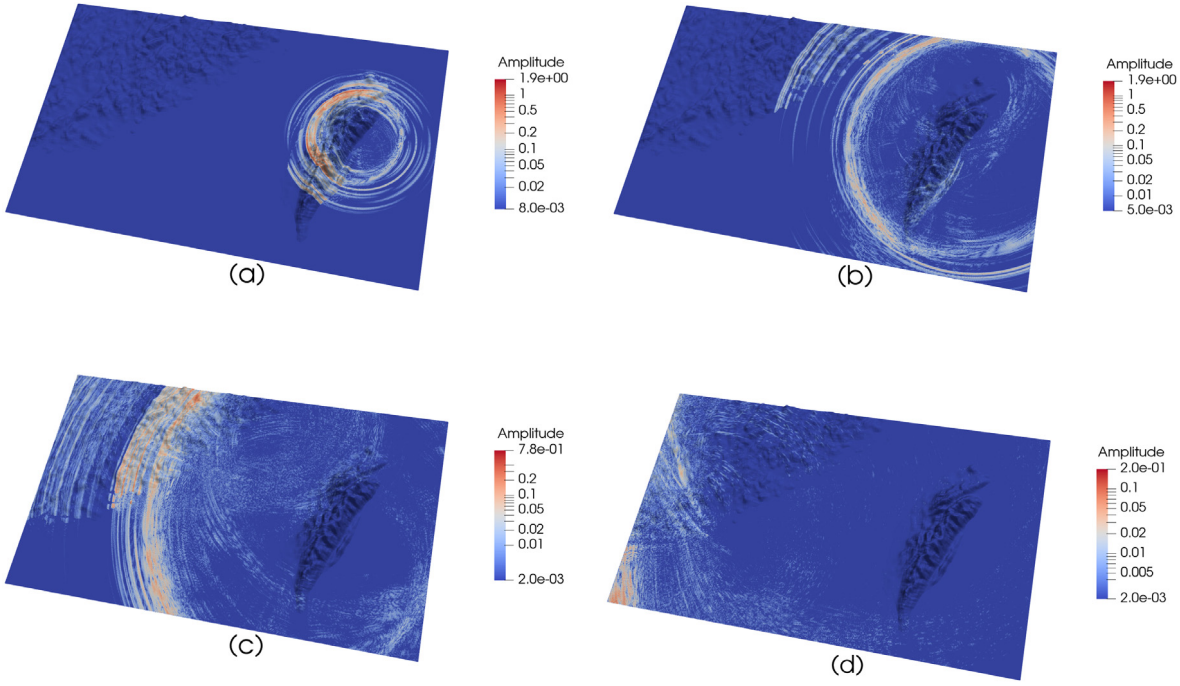

Fig. 14. The snapshot of displacement fields. (a) At time 48 s. (b) At time 120 s. (c) At time 216 s. (d) At time 360 s.

corresponding sampling density at 2 Hz are about 4.5, 6 and 7.5 PPW, respectively. The seismograms of the z-component in Kaohsiung station and Xiamen station are shown in Fig. 13(b) and (c), where it can be seen that the numerical results using $N = 4$ are almost indistinguishable compared with $N = 5$. The simulation using $N = 3$ is, however, significantly different from $N = 4$ and 5 at Xiamen station due to numerical dispersion, but the numerical dispersion in Kaohsiung station is significantly reduced because it has a shorter propagation distance. Hence, $N = 4$ is sufficient for accurate simulations of Hualien County event with realistic geological topography model. Furthermore, the NPML or PML domain accounts for only about 2% of the entire computational domain for $N = 4$. Table 3 also indicates that the NPML has higher computational efficiency than the standard PML. Finally, Figs. 14(a)–(d) show the snapshots at 48 s, 120 s, 216 s and 360 s of the norm of displacement field of the seismograms. Strong ground waves can be observed from these snapshots, and the ground waves of the out-going waves are well absorbed by

the NPML as illustrated in Figs. 14(b)–(d). This numerical example shows that the NPML and SEM can be applied in a large-scale seismic wave model with a realistic geological model.

6. Conclusion

In this paper, we have presented the Nearly PML formulation for FDTD and SEM simulations based upon the second-order wave equations with displacements-based scheme. First, the major advantage of the NPML technique is its simplicity in implementation because it does not modify the form of the governing wave equations, which makes the NPML very efficient and flexible to simulate wave propagation in elastic, anelastic and anisotropic materials. A computationally efficient NPML formulation can be evaluated by introducing 18 auxiliary variables, which are controlled by first-order ODEs that can easily be solved. Secondly, the NPML technique does not apply only to the elastic wave equation and acoustic wave equation, but also to Biot's poroelastic wave equation. Finally, the multiaxial PML method also can be introduced into the NPML scheme to avoid the intrinsic late-time instability of PML in some anisotropic materials.

Numerical tests indicate that the proposed NPML formulation has an excellent absorbing performance in elastic, anelastic and anisotropic materials, yet it requires less storage memory with easier implementation. The NPML system holds the excellent stability for the long-time simulation of wave propagation, even in a multiaxial NPML system.

Acknowledgments

This research was supported by the National Natural Science Foundation of China (grant number 61871462 and 61871340), and by the National R&D Projects for Key Scientific Instruments, China under Grant 2018YFC0603503. Special Program for Applied Research on Super Computation of the NSFC-Guangdong Joint Fund, China (the second phase) under Grant No. U1501501.

Appendix. Solution for the elastic wave Green's function in a isotropic homogeneous medium

The classical time-harmonic fundamental Green's function solution for an isotropic elastic solid [43] is

$$G_{pk}(\mathbf{x},\omega)=\frac{1}{4\pi\rho}\left\{\frac{1}{\omega^2}\partial_p\partial_k\left[\frac{e^{ik_s r}}{r}-\frac{e^{ik_p r}}{r}\right]+\frac{\delta_{pk}}{\tilde{v}_s^2}\frac{e^{ik_s r}}{r}\right\} \qquad k_p=\frac{\omega}{\tilde{v}_p} \qquad k_s=\frac{\omega}{\tilde{v}_s} \tag{A.1}$$

where G_{pk} is the 3-D frequency domain Green's function corresponds to the displacement field in the p direction produced by a point load applied at the k direction, k_p and k_s are the wavenumbers of the P-wave ($\tilde{v}_p$) and S-wave ($\tilde{v}_s$) in anelastic media, respectively. ω denotes the angular frequency, r is the distance between the source and the observation point.

For isotropic anelastic media, define the Q_p and Q_s to model attenuation corresponding to the compressional modulus and shear modulus, respectively [32]. These two moduli being complex in frequency domain, where the phase velocity is related to the real part of the elastic moduli and attenuation to their imaginary part. Kjartansson [35,46] derived exact analytical expressions for the complex modulus and phase velocity, which are valid for any positive value of quality factor, and over the full-frequency range. Following Kjartansson's method, we have

$$\gamma_N=\frac{1}{\pi}\arctan\frac{1}{Q_N}\quad(N=p,s) \qquad \tilde{N}(\omega)=N\cos^2\left(\frac{1}{2}\pi\gamma_N\right)\left(\frac{i\omega}{\omega_0}\right)^{2\gamma_N} \qquad \tilde{v}_N=\sqrt{\tilde{N}/\rho} \tag{A.2}$$

where N denotes either the P-wave modulus or shear modulus at the reference frequency ω_0, $\tilde{N}$ is complex modulus correspond to quality factor Q_N. It is noteworthy that $\tilde{N}$ is identical to N if the loss becomes zero ($Q\to\infty$). Then for a point force pulse $S(\omega)$ in the k-direction at the origin, the displacement field u_p in time domain is given by

$$u_p(\mathbf{x},t)=\mathcal{F}^{-1}\left[S(w)*G_{pk}(\mathbf{x},\omega)\right] \tag{A.3}$$

where $\mathcal{F}^{-1}$ is the inverse Fourier transform.

References

[1] Q.H. Liu, E. Schoen, F. Daube, C. Randall, H.L. Liu, P. Lee, J. Acoust. Soc. Am. 100 (1) (1996) 72–79.
[2] D. Komatitsch, C. Barnes, J. Tromp, Geophysics 65 (4) (2000) 1251–1260.
[3] U. Basu, Internat. J. Numer. Methods Engrg. 77 (2) (2010) 151–176.
[4] Q. Zhan, Q. Ren, Q. Sun, H. Chen, Q.H. Liu, IEEE Trans. Geosci. Remote Sens. 55 (3) (2017) 1254–1261.
[5] C. Deng, M. Luo, M. Yuan, B. Zhao, M. Zhuang, Q.H. Liu, J. Comput. Acoust. 26 (01) (2017) 1750031.
[6] Q. Zhan, Q. Ren, M. Zhuang, Q. Sun, Q.H. Liu, Comput. Method. Appl. M 329 (2018) 24–39.
[7] J.P. Berenger, Phys. Plasmas 114 (2) (1994) 185–200.
[8] W.C. Chew, Q.H. Liu, J. Comput. Acoust. 4 (4) (1996) 341–359.
[9] R. Martin, D. Komatitsch, S.D. Gedney, Comput. Model. Eng. Sci. 37 (3) (2008) 274–304.
[10] P.J. Matuszyk, C. Torres-Verdín, Comput. Math. Appl. 66 (11) (2013) 2335–2343.
[11] P. Ping, Y. Zhang, Y. Xu, J. Appl. Geophys. 101 (2014) 124–135.
[12] D. Komatitsch, R. Martin, Geophysics 72 (5) (2007) SM155–SM167.
[13] W. Zhang, Y. Shen, Geophysics 75 (4) (2010) T141–T154.
[14] K.C. Meza-Fajardo, A.S. Papageorgiou, Bull. Seismol. Soc. Am. 98 (4) (2008) 1811–1836.
[15] K. Gao, L. Huang, Geophysics 83 (1) (2018) T15–T30.
[16] Q.H. Liu, J. Acoust. Soc. Am. 105 (4) (1999) 2075–2084.
[17] G. Fan, Q.H. Liu, IEEE Antenn. Wirel. PR. 2 (1) (2003) 97–100.
[18] H. Wang, G. Tao, X. Shang, X. Fang, D.R. Burns, Appl. Geophys. 10 (4) (2013) 384–396.
[19] M. Zhuang, J. Zhou, S. Wei, Q.H. Liu, Geophys. Prospect. 66 (S1) (2018) 27–39.
[20] U. Basu, A.K. Chopra, Comput. Method Appl. M 192 (2003) 1337–1375.
[21] D. Komatitsch, J. Tromp, Geophys. J. Int. 154 (1) (2003) 146–153.
[22] U. Basu, A.K. Chopra, Internat. J. Numer. Methods Engrg. 59 (8) (2004) 1039–1074.
[23] G. Festa, J.P. Vilotte, Geophys. J. Int. 161 (3) (2005) 789–812.
[24] R. Matzen, Internat. J. Numer. Methods Engrg. 88 (10) (2011) 951–973.
[25] Z. Xie, D. Komatitsch, R. Martin, R. Matzen, Geophys. J. Int. 198 (3) (2014) 1714–1747.
[26] Z. Xie, R. Matzen, P. Cristini, D. Komatitsch, R. Martin, J. Acoust. Soc. Am. 140 (1) (2016) 165–175.
[27] S.A. Cummer, IEEE Microw. Wirel. Co. 13 (3) (2003) 128–130.
[28] J.P. Berenger, IEEE Microw. Wirel. Co. 14 (7) (2004) 334–336.
[29] J. Chen, Geophys. Prospect. 59 (4) (2011) 662–672.
[30] J. Chen, J. Zhao, Bull. Seismol. Soc. Am. 101 (6) (2011) 2866–2871.
[31] J. Chen, Can. J. Explor. Geophys. 37 (1) (2012) 22–27.
[32] Q. Zhan, M. Zhuang, Q. Sun, Q. Ren, Y. Ren, Y. Mao, Q.H. Liu, IEEE Geosci. Remote. S 55 (10) (2017) 5577–5584.
[33] Q. Liu, (Ph.D. thesis), California Institute of Technology, 2006.
[34] H.P. Liu, D.L. Anderson, H. Kanamori, Geophys. J. Int. 47 (1) (1976) 41–58.
[35] E. Kjartansson, J. Geophys. RES-SOL. EA. 84 (B9) (1979) 4737–4748.
[36] H. Emmerich, M. Korn, Geophysics 52 (9) (1987) 1252–1264.
[37] J.M. Carcione, Geophysics 58 (1) (1993) 110–120.
[38] B. Kaltenbacher, M. Kaltenbacher, I. Sim, J. Comput. Phys. 235 (2013) 407–422.
[39] T. Ohminato, B.A. Chouet, Bull. Seismol. Soc. Am. 87 (2) (1997) 494–515.
[40] P. Moczo, J. Kristek, L. Halada, Comenius University, Bratislava, 2004.
[41] P. Moczo, J. Kristek, L. Halada, Bull. Seismol. Soc. Am. 90 (3) (2000) 587–603.
[42] D. Komatitsch, S. Tsuboi, J. Tromp, Geophys. Monogr. 157 (2005) 205–227.
[43] C.Y. Wang, J.D. Achenbach, Proc. R. Soc. Lond. Ser. A Math. Phys. Eng. Sci. 449 (1937) (1995) 441–458.
[44] G. Mavko, T. Mukerji, J. Dvorkin, The Rock Physics Handbook: Tools for Seismic Analysis of Porous Media, Cambridge university press, 2009.
[45] E.H. Saenger, T. Bohlen, Geophysics 69 (2) (2004) 583–591.
[46] M. Zhuang, Q. Zhan, J. Zhou, N. Liu, Q.H. Liu, IEEE Trans. Geosci. Remote Sens. 57 (4) (2018) 2087–2096.